

All-dielectric antislot waveguide with subwavelength mode confinement and its high-efficiency coupling with input/output fiber

YUE Wen-Cheng^{1*}, WANG Qing^{1,2}, LI Xin-Yu^{1,3}, WANG Shu-Xiao^{1,2}, YU Ming-Bin^{1,4}

- (1. Laboratory of Silicon-Based Materials and Integrated Devices, Shanghai Institute of Microsystem and Information Technology, Chinese Academy of Sciences, Shanghai 200050, China;
2. University of Chinese Academy of Sciences, Beijing 100049, China;
3. Department of Electronic Engineering, Xi'an University of Technology, Xi'an 710048, China;
4. Shanghai Industrial μ Technology Research Institute, Shanghai 201800, China)

Abstract: Due to metallic ohmic loss, plasmonic waveguides usually have larger propagation loss. Here, an all-dielectric antislot waveguide was proposed, which can realize subwavelength mode confinement and theoretically lossless propagation simultaneously. A normalized mode area of 3.4×10^{-2} was achieved in the all-dielectric antislot waveguide. Moreover, an efficient coupling scheme between the small-size antislot waveguide and input/output fiber was proposed. An overall coupling efficiency of 92.7% was attained. The misalignment tolerance for 1 dB loss penalty was about $2 \mu\text{m}$ in both y and z directions.

Key words: photonic integrated circuits, nanophotonics, waveguide

PACS: 42.79.Gn, 42.82.-m, 42.82.Et

具有亚波长模式局域性的全介质反槽波导及其与输入/输出光纤的高效耦合

岳文成^{1*}, 王庆^{1,2}, 李欣雨^{1,3}, 王书晓^{1,2}, 余明斌^{1,4}

- (1. 中国科学院上海微系统与信息技术研究所, 硅基材料与集成器件实验室, 上海200050;
2. 中国科学院大学, 北京100049;
3. 西安理工大学 电子工程系, 西安710048;
4. 上海微技术工业研究院, 上海201800)

摘要: 由于金属固有的欧姆损耗, 表面等离子体波导通常具有较大的传输损耗。基于此, 提出了一种全介质反槽波导结构, 该波导可以同时实现亚波长模式局域性和理论上无损耗的传输, 归一化模式面积可以达到 3.4×10^{-2} 。另外, 为了实现该小尺寸反槽波导与输入/输出光纤的高效耦合, 提出了一种高效的耦合方案, 耦合效率可以达到 92.7%, 在 y 和 z 方向上 1 dB 损耗的耦合偏差均约为 $2 \mu\text{m}$ 。

关键词: 光子集成电路; 纳米光子学; 波导

中图分类号: O439 文献标识码: A

Introduction

In the highly informational age, it has become an inevitable trend to reduce the physical size of devices down to subwavelength scale to satisfy the growing demand for lower power consumption and higher data bandwidth of photonic devices^[1-2]. Confining light in subwavelength

scale can greatly enhance the light-matter interactions^[3-11], which can be used to realize ultra-compact low-threshold lasers^[6, 12-14], nonlinear enhancement^[15-16], high-efficient solar cells^[17-20], high-speed optical signal processing^[21-24], high-sensitivity sensors^[25-27], and so on. In recent years, in the realization of strong optical mode confinement, surface plasmon polaritons (SPPs)^[28-30]

Received date: 2020-11-18, **revised date:** 2021-05-12

收稿日期: 2020-11-18, **修回日期:** 2021-05-12

Foundation items: Supported by National Key Research and Development Program of China (2019YFB2203502), Shanghai Sailing Program (20YF1456900), Strategic Pioneer Research Projects of Defense Science and Technology (XDB43020500), and National Outstanding Youth Foundation of China (61904185)

Biography: YUE Wen-Cheng, female, PhD. Research area involves micro-nano photonic devices and silicon-based optoelectronic devices

* **Corresponding author:** E-mail: wencheng.yue@mail.sim.ac.cn

have gotten extensive attention. Photonic devices based on SPPs can break through the diffraction limit of light and allow for photonic integration with subwavelength mode confinement. However, stronger mode confinement of plasmonic waveguides is always accompanied by higher propagation loss. The trade-off between mode confinement and propagation loss is a typical challenge in plasmonic waveguides. The slot waveguide proposed by M. Lipson's group can guide and confine light in nanometer-size low-refractive-index material^[31-32]. However, the confinement is limited only in the direction perpendicular to the slot. In this article, an all-dielectric antislot waveguide was proposed in order to realize subwavelength mode confinement in the plane perpendicular to the direction of wave propagation. Because of excluding metal materials, all-dielectric waveguide has a natural advantage over its plasmonic counterparts in terms of propagation loss. Actually, subwavelength mode confinement and lossless propagation in theory can be achieved synchronously in the proposed antislot waveguide, conquering the trade-off between the two physical quantities. We also proposed an efficient scheme to improve the coupling efficiency between the small-size antislot waveguide and the input/output fiber.

1 Theoretical analysis

According to the first boundary condition of electromagnetic field, the continuity of the normal component of electric displacement vector, $D_{1n} = D_{2n}$ at the interface of two different materials, i. e., $\varepsilon_0 n_1^2 E_{1n} = \varepsilon_0 n_2^2 E_{2n}$, where n_1 and n_2 are the refractive index of the two different materials, respectively, and $n_1 < n_2$, subscript n is used to signify the normal component of electric field. Hence, the electric field near the interface at the low-index material side is enhanced by $(n_2/n_1)^2$ factors compared to that at the high-index material side, i. e., $E_{1n} = (n_2/n_1)^2 E_{2n}$. If the electric field is mainly along the normal direction and the low-index material region is small enough, then the electric field in the small-size low-index material region will be effectively enhanced. For nonmagnetic materials, the magnetic field is continuous at the interface of the two different materials. According to the formula of electromagnetic energy density

$$W(\mathbf{r}) = \frac{1}{2} \left[\varepsilon_0 n^2 |\mathbf{E}(\mathbf{r})|^2 + \mu_0 \mu_r |\mathbf{H}(\mathbf{r})|^2 \right], \quad (1)$$

the electromagnetic energy density in the small-size low-index material region W_1 will also be greater than that in the high-index material region W_2

$$\begin{aligned} W_1 &= \frac{1}{2} \left[\varepsilon_0 n_1^2 |E_{1n}|^2 + \mu_0 \mu_r |H_1|^2 \right] \\ &\approx \frac{1}{2} \left[\varepsilon_0 n_1^2 (n_2/n_1)^2 |E_{2n}|^2 + \mu_0 \mu_r |H_2|^2 \right] \\ &= \frac{1}{2} \left[\left(\frac{n_2^2}{n_1^2} \right) \varepsilon_0 n_2^2 |E_{2n}|^2 + \mu_0 \mu_r |H_2|^2 \right], \quad (2) \end{aligned}$$

$$W_2 = \frac{1}{2} \left[\varepsilon_0 n_2^2 |E_{2n}|^2 + \mu_0 \mu_r |H_2|^2 \right]. \quad (3)$$

Here, we suppose that the electric field is perpen-

dicular to the interface of the two different materials. Similarly, according to the second boundary condition of electromagnetic field, the continuity of the tangential component of electric field, at the interface of two different materials $E_{1t} = E_{2t}$, where subscript t is used to signify the tangential component of electric field. If the electric field is parallel to the interface of the two different materials, the electromagnetic energy density near the interface at the high-index material side W'_2 will be larger than that at the low-index material side W'_1

$$\begin{aligned} W'_2 &= \frac{1}{2} \left[\varepsilon_0 n_2^2 |E_{2t}|^2 + \mu_0 \mu_r |H_2|^2 \right] \\ &= \frac{1}{2} \left[\left(\frac{n_2^2}{n_1^2} \right) \varepsilon_0 n_1^2 |E_{1t}|^2 + \mu_0 \mu_r |H_1|^2 \right], \quad (4) \end{aligned}$$

$$W'_1 = \frac{1}{2} \left[\varepsilon_0 n_1^2 |E_{1t}|^2 + \mu_0 \mu_r |H_1|^2 \right]. \quad (5)$$

If the high-index material region is small enough, then the electromagnetic energy density in the whole small-size high-index material region will be enhanced effectively.

2 Results and discussions

2.1 Properties of the all-dielectric antislot waveguide

The three-dimensional (3D) structural diagram and the cross-section of the antislot waveguide are shown in Figs. 1(a-b), respectively. We studied the influence of structural parameters on mode confinement by the finite element method (FEM) at $\lambda = 1550$ nm, as shown in Fig. 2(a). In the normalized mode area A_{eff}/A_0 , $A_0 = \lambda^2/4$ is the diffraction-limited mode area and A_{eff} is mode area given by^[7]

$$A_{\text{eff}} = \frac{1}{\max\{W(\mathbf{r})\}} \iint W(\mathbf{r}) d^2\mathbf{r}, \quad (6)$$

where $W(\mathbf{r})$ is the electromagnetic energy density given by Eq. 1. The refractive index of silicon and silica at the wavelength of 1550 nm is 3.476 and 1.444, respectively.

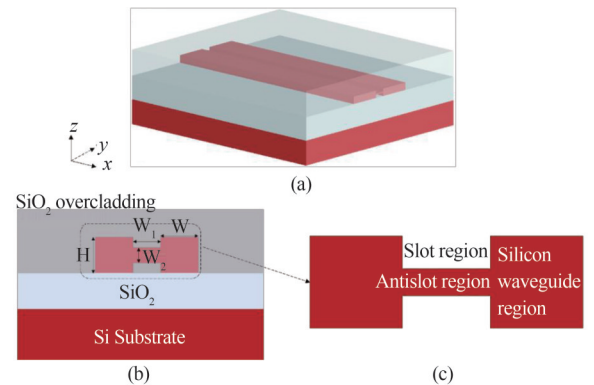


Fig. 1 (a) Three-dimensional structural diagram of the all-dielectric antislot waveguide, (b) its cross-section, (c) partial enlarged view of (b)

Note: (a), (b), and (c) are all not drawn to scale

图1 (a) 全介质反槽波导的三维结构示意图, (b) 截面图, (c) 图(b)的局部放大图

注: (a)、(b)、和(c)均未按比例绘制

ly. A normalized mode area of 3.4×10^{-2} is achieved at $W = 150$ nm, $W_1 = 50$ nm, and $W_2 = 20$ nm, which is on the same order of magnitude as that of the plasmonic waveguides. The normalized electromagnetic energy density and electric vector distributions at these parameters are shown in Fig. 2(b). We can clearly see that electromagnetic energy is tightly confined in the nanoscale antislot region. The strong mode confinement is attributed to the electromagnetic orthogonal boundary conditions. As discussed in Sect. 2, because the electric vector [white arrows in Fig. 2(b)] is perpendicular to the interface of the slot and the silicon waveguide and the low-index slot region [Fig. 1(c)] is nanoscale in size, the electromagnetic energy density in the whole slot region is enhanced compared to that in the silicon waveguide region [Fig. 1(c)] according to the first boundary condition of electromagnetic field. Similarly, because the electric vector is parallel to the interface of the antislot and the slot and the size of the high-index antislot region [Fig. 1(c)] is also nanoscale, the electromagnetic energy density in the whole antislot region is greater than that in the slot region according to the second boundary condition. As shown by the white arrows in Fig. 2(b), the electric field is along with the y -direction which indicates the guided mode of the antislot waveguide is a quasi-TE mode. The quasi-TE mode is an eigenmode of the antislot waveguide and because the all-dielectric antislot waveguide does not contain metal, the quasi-TE eigenmode is theoretically lossless, which is consistent with our calculated results by the FEM, the negligible imaginary part of the effective refractive index. The theoretically lossless propagation of the all-dielectric antislot waveguide is a significant breakthrough compared with its plasmonic counterparts. Subwavelength mode confinement and theoretically lossless propagation can be achieved simultaneously in a single all-dielectric antislot waveguide, overcoming the trade-off between the two physical quantities.

2.2 Coupling between the antislot waveguide and input/output fiber

A lot of applications can be achieved when light is confined in deep subwavelength scale, but due to the serious mode mismatch, the direct coupling between the input/output fiber and the small-size antislot waveguide is usually inefficient. Here, we proposed an efficient coupling scheme to improve the coupling efficiency. The whole light coupling structure is given by Fig. 3. The light from a fiber couples to a silicon waveguide through a conventional inverse taper firstly, then it transmits from the silicon waveguide to the antislot waveguide through an adiabatic linear taper coupler whose size gradually changes from that of the silicon waveguide to that of the antislot waveguide. The fiber used here is a lensed fiber with a $2.9 \mu\text{m}$ mode-field diameter (MFD)^[33]. The height, width, and length of the silicon waveguide are 220 nm, 350 nm, and $2 \mu\text{m}$, respectively. The inverse taper has an 80 nm wide tip^[33] and is embedded in a polymer waveguide. The polymer waveguide has a cross section of $3 \mu\text{m} \times 3 \mu\text{m}$ which is matched to that of the lensed fiber. The structural parameters of the antislot waveguide

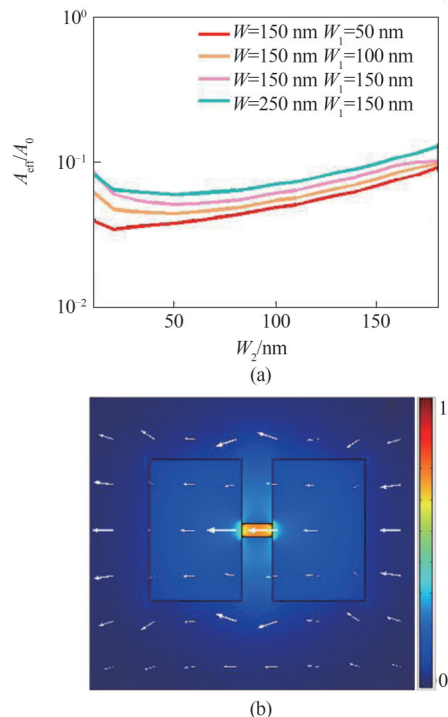


Fig. 2 (a) Influence of structural parameters on normalized mode area of the all-dielectric antislot waveguide, (b) normalized electromagnetic energy density and electric vector distributions at $W = 150$ nm, $W_1 = 50$ nm, and $W_2 = 20$ nm. The definition of W , W_1 , and W_2 is shown in Fig. 1(b)

Note: The height of the waveguide is 220 nm

图2 (a) 全介质反槽波导的结构参数变化对归一化模式面积的影响, (b) 在 $W = 150$ nm、 $W_1 = 50$ nm、 $W_2 = 20$ nm 的参数取值下, 归一化电磁场能量密度和电矢量的分布情况, 其中 W 、 W_1 、和 W_2 的定义如图 1(b) 所示

注: 波导的高度为 220 nm

used here are the same as above. The refractive index of the polymer is 1.5 at $\lambda = 1550$ nm and other material parameters are the same as above. We firstly optimized the position of the lensed fiber by calculating the overlap between the fiber mode and the fundamental TE mode of the polymer waveguide using the finite difference eigenmode (FDE) solver in commercial software Lumerical MODE. An optimal 94.6% (0.24 dB) overlap is achieved at $y = 0$ and $z = 1.4 \mu\text{m}$, and the misalignment tolerance for 1 dB loss penalty is about $2 \mu\text{m}$ in both y and z directions (Fig. 4). Then, we optimized the length of the inverse taper and the adiabatic linear taper using the eigenmode expansion (EME) solver in MODE for improving the coupling efficiency further. Figures 5 (a-b) show the coupling efficiency from the lensed fiber to the silicon waveguide with the lensed fiber at the optimal position and from the silicon waveguide to the antislot waveguide, respectively. The coupling efficiency from the lensed fiber to the silicon waveguide increases along with the length of the inverse taper firstly and then tends to be stable. A coupling efficiency of 92.8% is achieved at a length of $150 \mu\text{m}$, which includes the overlap loss of the fiber and the polymer waveguide. The coupling efficiency from the silicon waveguide to the antislot waveguide is very high even when the adiabatic linear ta-

per is very short. A coupling efficiency of 97.7% is attained even without the adiabatic linear taper and it can reach up to 99.9% when the adiabatic linear taper is 8 μm . The adiabatic linear taper is mainly used to reduce the reflection from the silicon waveguide to the antislot waveguide caused by structural change abruptly, thus reducing the wave oscillation back and forth and avoiding the interference of incident wave and reflected wave. The electromagnetic energy transfer process from the silicon waveguide to the antislot waveguide is shown in Fig. 6, where (a) and (b) correspond to the case when the length of the adiabatic linear taper is 8 μm , (c) and (d) are the case of without the adiabatic linear taper. Clearly, the electromagnetic energy can be effectively coupled to the nanoscale antislot region of the antislot waveguide in the two cases. However, there are standing waves in the silicon waveguide in the case of without the adiabatic linear taper, which agrees well with the above statement. An overall coupling efficiency of 92.7% from the lensed fiber to the small-size antislot waveguide is achieved with 150 μm inverse taper and 8 μm adiabatic linear taper. This corresponds to an overall coupling loss of 0.33 dB.

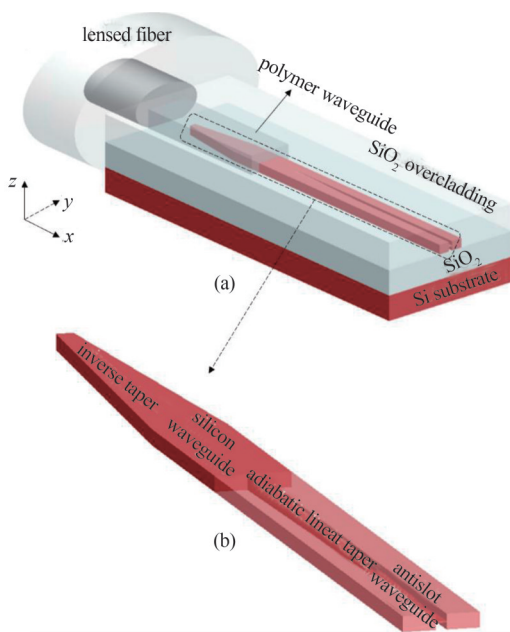


Fig. 3 (a) The light coupling structure from the lensed fiber to the antislot waveguide or vice versa, (b) partial enlarged view of (a)
 Note: (a) and (b) are both not drawn to scale. The zero in y and z directions is located at the middle of the coupling structure and the middle of the top silicon, respectively
 图3 (a) 从锥形光纤到反槽波导或从反槽波导到锥形光纤的耦合结构示意图, (b) 图(a)的局部放大图
 注: (a)和(b)均未按比例绘制。 y 和 z 方向的坐标零点分别位于耦合结构的中心和顶层硅的中心

The whole electromagnetic energy transfer process from the antislot waveguide to the output end is shown in Fig. 7(a), where the length of the antislot waveguide, the adiabatic linear taper, the silicon waveguide and the inverse taper is 4 μm , 8 μm , 2 μm and 10 μm , respectively. To save simulation time, the length of the inverse

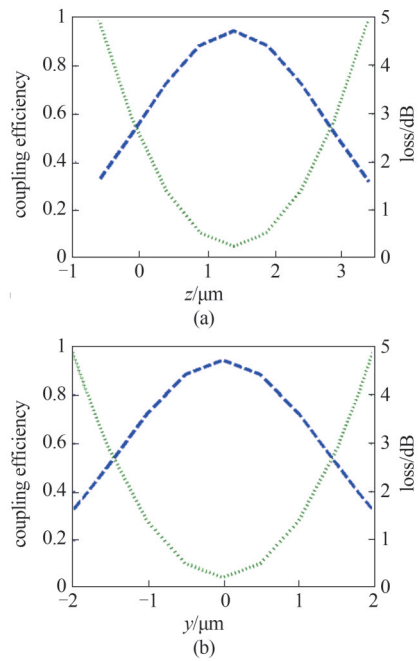


Fig. 4 Influence of the lensed fiber position on coupling efficiency and loss in (a) z and (b) y directions. The optimal fiber position in z and y directions is approximately located at 1.4 μm and 0, respectively

图4 锥形光纤在(a) z 方向和(b) y 方向上的位置变化对耦合效率和损耗的影响。最优的光纤位置在 z 方向和 y 方向上分别位于约1.4 μm 处和0处

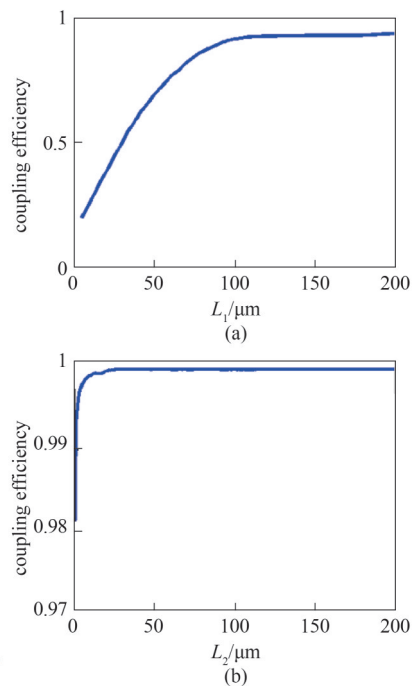


Fig. 5 Coupling efficiency (a) from the lensed fiber to the silicon waveguide as a function of the inverse taper length (L_1) with the lensed fiber at the optimal position and (b) from the silicon waveguide to the antislot waveguide as a function of the adiabatic linear taper length (L_2)

图5 (a) 锥形光纤位于最优位置时, 从锥形光纤到硅波导的耦合效率随倒锥形耦合器长度(L_1)的变化关系, (b) 从硅波导到反槽波导的耦合效率随绝热线性锥形耦合器长度(L_2)的变化关系

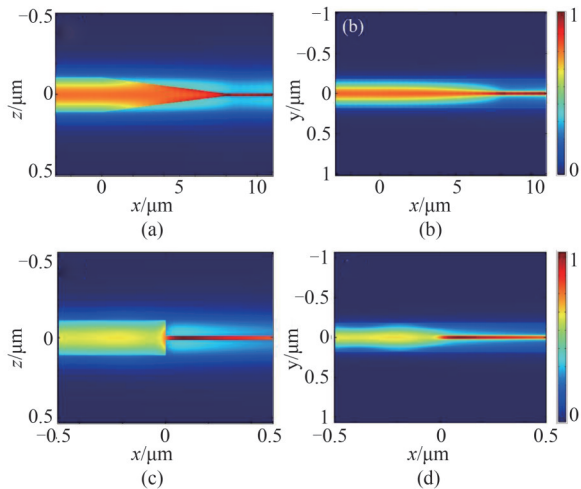


Fig. 6 Electromagnetic energy transfer process from the silicon waveguide to the antislot waveguide (a), (c) at the xz section with $y = 0$, (b), (d) at the xy section with $z = 0$

Note: (a) and (b) correspond to the case when the length of the adiabatic linear taper is $8 \mu\text{m}$, (c) and (d) are the case of without the adiabatic linear taper

图6 (a)、(c) 在 $y = 0$ 的 xz 截面上电磁场能量从硅波导到反槽波导的传输过程, (b)、(d) 在 $z = 0$ 的 xy 截面上电磁场能量从硅波导到反槽波导的传输过程

注: (a)和(b)对应绝热线性锥形耦合器的长度为 $8 \mu\text{m}$ 时的情况, (c)和(d)是没有绝热线性锥形耦合器时的情况

taper here is set to $10 \mu\text{m}$ only to qualitatively exhibit the electromagnetic energy transfer process. The electromagnetic energy can be effectively coupled from the antislot waveguide to the output end. To illustrate the role of the adiabatic linear taper, Fig. 7(b) demonstrates the coupling process from the antislot waveguide to the output end without the adiabatic linear taper. Clearly, there is macroscopic reflection at the interface of the antislot waveguide and the silicon waveguide in the case of without the adiabatic linear taper, which further indicates the adiabatic linear taper can be used to reduce the reflection and avoid the interference of incident wave and reflected wave, mentioned above.

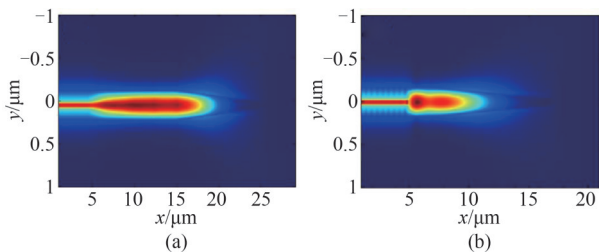


Fig. 7 Electromagnetic energy transfer process from the antislot waveguide to the output end (a) the length of the antislot waveguide, the adiabatic linear taper, the silicon waveguide and the inverse taper is $4 \mu\text{m}$, $8 \mu\text{m}$, $2 \mu\text{m}$ and $10 \mu\text{m}$, respectively, (b) corresponds to the case of without the adiabatic linear taper

图7 电磁场能量从反槽波导到输出端的传输过程 (a)图中反槽波导、绝热线性锥形耦合器、硅波导、和倒锥形耦合器的长度分别为 $4 \mu\text{m}$ 、 $8 \mu\text{m}$ 、 $2 \mu\text{m}$ 、和 $10 \mu\text{m}$, (b)图对应没有绝热线性锥形耦合器的情况

3 Conclusion

We have demonstrated an all-dielectric antislot waveguide which can confine light into nanoscale antislot region. A normalized mode area of 3.4×10^{-2} is achieved at the wavelength of 1550nm , which is on the same order of magnitude as that of the plasmonic waveguides. The strong mode confinement results from the electromagnetic orthogonal boundary conditions. Because the all-dielectric antislot waveguide does not contain metal, its supported quasi-TE eigenmode can propagate without loss in theory, which is a significant breakthrough compared with its plasmonic counterparts. The proposed all-dielectric antislot waveguide realizes subwavelength mode confinement and theoretically lossless propagation simultaneously, conquering the trade-off between the two physical quantities. On the other hand, a high-efficiency coupling scheme between the small-size antislot waveguide and the input/output fiber has also been proposed. The overall coupling efficiency of 92.7% can be obtained with $150 \mu\text{m}$ inverse taper and $8 \mu\text{m}$ adiabatic linear taper. The misalignment tolerance for 1dB loss penalty is about $2 \mu\text{m}$ in both y and z directions. The excellent properties make the antislot waveguide have great application potential in many fields, such as increasing the integration density of photonic integrated circuits^[34], improving the sensitivity of photonic sensing^[35], and enhancing the fluorescence signals in bioimaging^[36].

References

- [1] Kirchain R, Kimerling L. A roadmap for nanophotonics [J]. *Nat. Photon.* 2007, **1**(6): 303–305.
- [2] Welch D F, Kish F A, Nagarajan R, *et al.* The realization of large-scale photonic integrated circuits and the associated impact on fiber-optic communication systems [J]. *J. Lightwave Tech.* 2006, **24**(12): 4674–4683.
- [3] Maier S A. *Plasmonics: fundamentals and applications* [M]. Springer New York, 2007.
- [4] Maier S A, Kik P G, Atwater H A. Observation of coupled plasmon-polariton modes in Au nanoparticle chain waveguides of different lengths: estimation of waveguide loss [J]. *Appl. Phys. Lett.* 2002, **81**(9): 1714–1716.
- [5] Pyayt A L, Wiley B, Xia Y, *et al.* Integration of photonic and silver nanowire plasmonic waveguides [J]. *Nat. Nanotech.* 2008, **3**(11): 660–665.
- [6] Oulton R F, Sorger V J, Zentgraf T, *et al.* Plasmon lasers at deep subwavelength scale [J]. *Nature*, 2009, **461**: 629–632.
- [7] Oulton R F, Sorger V J, Genov D A, *et al.* A hybrid plasmonic waveguide for subwavelength confinement and long-range propagation [J]. *Nat. Photon.* 2008, **2**: 496–500.
- [8] Gramotnev D K, Bozhevolnyi S I. Plasmonics beyond the diffraction limit [J]. *Nat. Photon.* 2010, **4**(2): 83–91.
- [9] Hill M T, Oei Y S, Smalbrugge B, *et al.* Lasing in metallic-coated nanocavities [J]. *Nat. Photon.* 2007, **1**(10): 589–594.
- [10] Krasavin A V, Zayats A V. Silicon-based plasmonic waveguides [J]. *Opt. Express*, 2010, **18**(11): 11791–11799.
- [11] Oulton R F, Bartal G, Pile D F P, *et al.* Confinement and propagation characteristics of subwavelength plasmonic modes [J]. *J. New Phys.* 2008, **10**(10): 105018–105018.
- [12] Matsuo S, Shinya A, Kakitsuka T, *et al.* High-speed ultracompact buried heterostructure photonic-crystal laser with 13fJ of energy consumed per bit transmitted [J]. *Nat. Photon.* 2010, **4**(9): 648–654.
- [13] Takahashi Y, Inui Y, Chihara M, *et al.* A micrometre-scale Raman silicon laser with a microwatt threshold [J]. *Nature*, 2013, **498**(7455): 470–474.
- [14] Noda S, Fujita M, Asano T. Spontaneous-emission control by photonic crystals and nanocavities [J]. *Nat. Photon.* 2007, **1**: 449–458.

- [15] Kim S, Jin J, Kim Y J, *et al.* High-harmonic generation by resonant plasmon field enhancement [J]. *Nature*, 2008, **453** (7196): 757-760.
- [16] Nozaki K, Shinya A, Matsuo S, *et al.* Ultralow-power all-optical RAM based on nanocavities [J]. *Nat. Photon.* 2012, **6**(4): 248-252.
- [17] Atwater H A, Polman A. Plasmonics for improved photovoltaic devices [J]. *Nat. Mater.* 2010, **9**(3): 205-213.
- [18] Green M A, Pillai S. Harnessing plasmonics for solar cells [J]. *Nat. Photon.* 2012, **6**(3): 130-132.
- [19] Brongersma M L, Cui Y, Fan S. Light management for photovoltaics using high-index nanostructures [J]. *Nat. Mater.* 2014, **13** (5): 451-460.
- [20] Schuller J A, Barnard E S, Cai W, *et al.* Plasmonics for extreme light concentration and manipulation [J]. *Nat. Mater.* 2010, **9**(4): 193-204.
- [21] Reed G T, Mashanovich G, Gardes F Y, *et al.* Silicon optical modulators [J]. *Nat. Photon.* 2010, **4**(8): 518-526.
- [22] Nozaki K, Tanabe T, Shinya A, *et al.* Sub-femtojoule all-optical switching using a photonic-crystal nanocavity [J]. *Nat. Photon.* 2010, **4**, 477-483.
- [23] Melikyan A, Alloatti L, Muslija A, *et al.* High-speed plasmonic phase modulators [J]. *Nat. Photon.* 2014, **8**(3): 229-233.
- [24] Xu Q, Schmidt B, Pradhan S, *et al.* Micrometre-scale silicon electro-optic modulator [J]. *Nature*, 2005, **435**(7040): 325-327.
- [25] Brolo A G. Plasmonics for future biosensors [J]. *Nat. Photon.* 2012, **6**(11): 709-713.
- [26] Chakravarty S, Lai W C, Zou Y, *et al.* Multiplexed specific label-free detection of NCI-H358 lung cancer cell line lysates with silicon based photonic crystal microcavity biosensors [J]. *Biosens. Bioelectron.* 2013, **43**(1): 50-55.
- [27] Hu S, Zhao Y, Qin K, *et al.* Enhancing the sensitivity of label-free silicon photonic biosensors through increased probe molecule density [J]. *ACS Photon.* 2014, **1**(7): 590-597.
- [28] Dittlacher H, Krenn J R, Schider G, *et al.* Two-dimensional optics with surface plasmon polaritons [J]. *Appl. Phys. Lett.* 2002, **81**(10): 1762-1764.
- [29] Zayats A V, Smolyaninov I I, Maradudin A A. Nano-optics of surface plasmon polaritons [J]. *Phys. Rep.* 2005, **408**(3-4): 131-314.
- [30] Raether H. Surface plasmons on smooth and rough surfaces and on gratings [M]. Springer Berlin Heidelberg, 1988.
- [31] Almeida V R, Xu Q, Barrios C A, *et al.* Guiding and confining light in void nanostructure [J]. *Opt. Lett.* 2004, **29**(11): 1209-1211.
- [32] Xu Q, Almeida V R, Panepucci R R, *et al.* Experimental demonstration of guiding and confining light in nanometer-size low-refractive-index material [J]. *Opt. Lett.* 2004, **29**(14): 1626-1628.
- [33] Pu M, Liu L, Ou H, *et al.* Ultra-low-loss inverted taper coupler for silicon-on-insulator ridge waveguide [J]. *Opt. Commun.* 2010, **283** (19): 3678-3682.
- [34] Ebbesen T W, Genet C, Bozhevolnyi S I. Surface-plasmon circuitry [J]. *Phys. Today*, 2008, **61**(5): 44-50.
- [35] Dell'Olio F, Passaro V M. Optical sensing by optimized silicon slot waveguides [J]. *Opt. Express*, 2007, **15**(8): 4977-4993.
- [36] Guo Z, Park S, Yoon J, *et al.* Recent progress in the development of near-infrared fluorescent probes for bioimaging applications [J]. *Chem. Soc. Rev.* 2013, **43**(1): 16-29.